

Kinetics of the Gas-Phase Recombination Reaction of Hydroxyl Radicals to Form Hydrogen Peroxide[†]

Stig R. Sellevåg,^{*,‡,⊥} Yuri Georgievskii,[§] and James A. Miller^{*,§}

SINTEF Energy Research, N-7465 Trondheim, Norway, and Combustion Research Facility, Sandia National Laboratories, Livermore, California 94551-0969

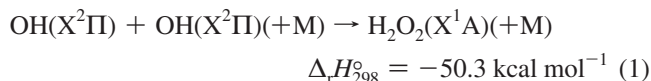
Received: December 15, 2008; Revised Manuscript Received: January 30, 2009

The potential energy hypersurface (PES) of the reaction $\text{OH} + \text{OH} (+\text{M}) \rightarrow \text{H}_2\text{O}_2 (+\text{M})$ has been investigated at the CASPT2/aug-cc-pVDZ and CASPT2/aug-cc-pVTZ levels of theory. The PES is characterized by a barrier below the energy of the reactants and a hydrogen-bonded adduct formed by the OH radicals. On the basis of the potential energy hypersurface obtained, the high-pressure limiting rate coefficient (k_∞) of the reaction was calculated using variable reaction coordinate transition-state theory, classical trajectory simulations, and a two-transition-state model. Over the temperature range of 200–3000 K, $k_\infty(T) = 9.3 \times 10^{-9} T^{-1.040} \exp(3.5/T) + 1.13 \times 10^{-12} T^{0.303} \exp(84/T) \text{ cm}^3 \text{ molecule}^{-1} \text{ s}^{-1}$ is reported. Available experimental data on the pressure dependence of the reaction with He and Ar as bath gases were analyzed using a two-dimensional master equation. Over the temperature range of 200–3000 K, the following low-pressure limiting rate coefficient (k_0) and center broadening factor (F_{cent}) were obtained for He as the bath gas: $k_0(T) = 4.4 \times 10^{-20} T^{-4.30} \exp(-340/T) \text{ cm}^6 \text{ molecule}^{-2} \text{ s}^{-1}$ and $F_{\text{cent}} = 0.54$. For the dissociation of H_2O_2 in Ar, the following values are reported over the temperature range of 500–3000 K: $k_0(T) = 1.4 \times 10^8 T^{-4.57} \exp(-26322/T) \text{ cm}^3 \text{ molecule}^{-1} \text{ s}^{-1}$ and $F_{\text{cent}} = 0.55$. The calculations describe all experimental data well, except the observations at 210 K for the reaction with He as the bath gas.

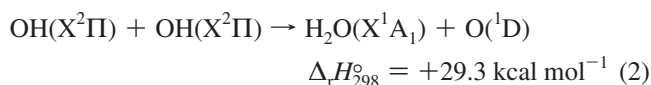
1. Introduction

Carbon dioxide (CO_2) capture and storage technologies may significantly reduce CO_2 emissions from the power production industry. One of the technologies considered is the so-called precombustion system where hydrogen (H_2), manufactured from coal or natural gas, is used as gas turbine fuel. The separated CO_2 is subsequently stored. To enable use of H_2 as gas turbine fuel, an accurate description of the combustion process at elevated pressures is needed. It has been shown, however, that apparently small differences between available chemical mechanisms for H_2 combustion can have a substantial effect on predicted flame properties.^{1–3}

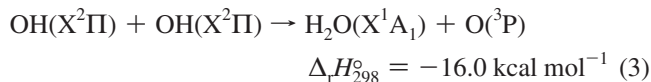
Reactions involving hydrogen peroxide (H_2O_2) are of importance for describing the autoignition of hydrogen and hydrocarbons in air, especially at elevated pressures.^{4–7} In this article, our focus is on the gas-phase recombination of hydroxyl (OH) radicals to form H_2O_2



This reaction competes with the bimolecular reaction



which takes place on the singlet H_2O_2 potential energy hypersurface (PES) and the reaction



which takes place on the triplet H_2O_2 PES (the enthalpies of reaction at 298 K, $\Delta_r H_{298}^\circ$, have been calculated from enthalpies of formation⁸).

Several experimental studies of the kinetics of reaction 1 have been reported in the literature.^{9–14} Trainor and von Rosenberg¹⁰ measured the low-pressure limiting rate coefficient, $k_0(T)$ of reaction 1 with N_2 as the bath gas and reported $k_{1,0}(298 \text{ K}) = (2.5 \pm 0.3) \times 10^{-31} \text{ cm}^6 \text{ molecule}^{-2} \text{ s}^{-1}$. The same reaction was also investigated by Zellner et al.¹¹ over the temperature range of 253–353 K. Their experimental data could be described by $k_{1,0} = 6.9 \times 10^{-31} (T/298 \text{ K})^{-0.8} \text{ cm}^6 \text{ molecule}^{-2} \text{ s}^{-1}$, $k_{1,\infty} = 1.5 \times 10^{-11} \text{ cm}^3 \text{ molecule}^{-1} \text{ s}^{-1}$, and $F_{1,\text{cent}} = 0.6$, where k_∞ is the high-pressure limiting rate coefficient and F_{cent} is the center broadening factor.¹⁵ Zellner and co-workers also investigated reaction 1 using water as the bath gas. Forster et al.¹² performed saturated laser-induced fluorescence measurements of the same reaction for pressures between 1 and 150 bar of He at 298 K. The falloff curve obtained could be described by $k_{1,0} = 3.7 \times 10^{-31} \text{ cm}^6 \text{ molecule}^{-2} \text{ s}^{-1}$, $k_{1,\infty} = 2.2 \times 10^{-11} \text{ cm}^3 \text{ molecule}^{-1} \text{ s}^{-1}$, and $F_{1,\text{cent}} = 0.6$. The measurements of Forster and colleagues were extended by Fulle et al.¹³ On the basis of extrapolation of the falloff curves obtained, Fulle and co-workers

[†] Part of the “George C. Schatz Festschrift”.

^{*} To whom correspondence should be addressed. E-mail: s.r.sellevag@kjemi.uio.no (S.R.S.); jamille@sandia.gov (J.A.M.).

[‡] SINTEF Energy Research.

[§] Sandia National Laboratories.

[⊥] Present address: Center for Materials Science and Nanotechnology, University of Oslo, P.O. Box 1126 Blindern, N-0318 Oslo, Norway.

reported $k_{1,\infty} = (2.6 \pm 0.8) \times 10^{-11} (T/300 \text{ K})^{0 \pm 0.5} \text{ cm}^3 \text{ molecule}^{-1} \text{ s}^{-1}$ over the temperature range of 200–400 K. Unfortunately, because of the competition between reactions 1 and 3, falloff extrapolations toward the high-pressure limit of reaction 1 become very difficult for temperatures above 400 K with present-day technologies.¹³

To our knowledge, there is no experimental data on the kinetics of reaction 1 at temperatures relevant for combustion. There is, however, experimental data on the dissociation of H_2O_2 with Ar as the bath gas. From shock tube measurements, Kappel et al.¹⁴ reported $k_{-1,0} = 3.8 \times 10^{-8} \exp(-21962/T) \text{ cm}^3 \text{ molecule}^{-1} \text{ s}^{-1}$ over the temperature range of 950–1250 K. For earlier studies of $k_{-1,0}$, we refer to Baulch et al.⁸ for a review.

If we look at theoretical investigations of reaction 1, the nature of the long-range interaction potential was first discussed by Benson¹⁶ and later investigated by Harding¹⁷ using multireference configuration-interaction (MRCI) calculations. Koput et al.¹⁸ and Kuhn et al.¹⁹ have constructed six-dimensional analytical potential energy hypersurfaces for the electronic ground state of hydrogen peroxide. Troe²⁰ has calculated strong collision low-pressure limiting rate coefficients for the dissociation of H_2O_2 immersed in Ar. Brouwer and co-workers²¹ investigated the dissociation of hydrogen peroxide by means of simplified and detailed statistical adiabatic channel models (SACM); however, simple model potentials were employed in the calculations. Detailed SACM calculations were also carried out by Maergoiz et al.²² employing an electrostatic and polarization potential. The high-pressure limiting rate coefficient was, however, only calculated for temperatures up to 55 K. Troe and Ushakov²³ have recently performed a SACM and classical trajectory study of reaction 1 using the PES constructed by Kuhn and co-workers.¹⁹ Over the temperature range of 60–1500 K, Troe and Ushakov obtained $k_{1,\infty} = [0.376(298 \text{ K}/T)^{0.47} + 0.013(T/298 \text{ K})^{0.74}] \times 10^{-10} \text{ cm}^3 \text{ molecule}^{-1} \text{ s}^{-1}$. Brouwer et al.²¹ have investigated the dissociation of hydrogen peroxide using SACM and SACM-modified phase space theory. However, a simple model potential was used in the calculations.

For combustion modeling purposes, there is a need to extend the available rate data on reaction 1 to higher temperatures. To achieve this objective, we have investigated the ground-state potential energy hypersurface of the reaction by means of high-level ab initio methods. Variable reaction coordinate transition-state theory, classical trajectory simulations, and a two-transition-state model have been used to calculate the high-pressure limiting rate coefficient. A two-dimensional master equation was used to characterize the falloff behavior of reaction 1 and to calculate its low-pressure limiting rate coefficient.

2. Computational Methods

2.1. Electronic Structure Calculations. The electronic ground-state potential energy hypersurface (PES) of reaction 1 was investigated using the complete-active-space, self-consistent field (CASSCF) method of Knowles and Werner.^{24,25} The active space consisted of six electrons distributed in four oxygen p orbitals, hereafter denoted as CAS(6,4). Dynamical electron correlation was included using multistate, multireference complete-active-space, second-order (MS-MR-CASPT2) perturbation theory;^{26,27} the four lowest states of the H_2O_2 complex were averaged. Reference energies of reactants were obtained using a supermolecule approach. The CASSCF and MS-MR-CASPT2 calculations were carried out with the MOLPRO package.²⁸ In the following, the MS-MR-CASPT2 method will be referred to as CASPT2 for brevity.

Additional calculations were carried out with the Becke three-parameter,²⁹ Lee–Yang–Parr³⁰ (B3LYP) hybrid functional,

Møller–Plesset second-order perturbation theory (MP2),³¹ and coupled-cluster singles and doubles theory with perturbational triples corrections [CCSD(T)].³² The B3LYP and CCSD(T) calculations were carried out using the Gaussian 98 suite of programs.³³ Anharmonic zero-point vibrational energies (ZPE) of stationary points were calculated with the MP2 model implemented in GAMESS.^{34,35}

Dunning's correlation-consistent aug-cc-pVXZ ($X = \text{D, T, Q, 5}$)^{36–38} basis sets were employed in the calculations. Single-point correlation energies were extrapolated toward the basis set limit using the extrapolation scheme of Halkier et al.³⁹ (eq 4)

$$E_{XY}^{\infty} = \frac{X^3 E_X - Y^3 E_Y}{X^3 - Y^3} \quad (4)$$

where E_X is the correlation energy obtained with the highest cardinal number X and E_Y is the correlation energy obtained with cardinal number $Y = X - 1$. In the rest of the paper, such calculations will be referred to, for example, as CCSD(T)/EBXY, with EB being short for extrapolated basis. The Pople-style 6-31G* basis set was employed in some of the calculations.

2.2. Variable Reaction Coordinate Transition-State Theory. The high-pressure limiting rate coefficient (k_{∞}) of reaction 1 for a given temperature (T) was evaluated from eq 5

$$k_{\infty}(T) = f_{\text{el}}^{\text{reac}} \frac{1}{\sigma^{\ddagger} h Q_{\text{reac}}(T)} \int N^{\ddagger}(E, J) \exp(-E/k_{\text{B}}T) dE dJ \quad (5)$$

where the labels reac and \ddagger denote that the quantities are for the reactants and the transition state (TS), respectively. Here, h is Planck's constant, k_{B} is the Boltzmann constant, f_{el} is a function of the electronic partition functions of the reactants and the TS, σ is the rotational symmetry number, $Q_{\text{reac}}(T)$ is the canonical partition function of the reactants, and $N^{\ddagger}(E, J)$ is the number of states of the TS for a given energy E and total angular momentum quantum number J . The translational, rotational, and vibrational modes of the reaction system were assumed to be separable into sets of translational and conserved modes.⁴⁰ The rotational partition functions were approximated by their classical limits, and the number of states of the TS was calculated from variable reaction coordinate transition-state theory (VRC-TST)^{41,42} considering only contributions from the transitional modes. Within VRC-TST, dividing surfaces are defined in terms of a fixed distance between pivot points on each fragment, and both the location and the separation between the pivot points are varied to determine the minimum reactive flux through a dividing surface. The reactive flux through a dividing surface was determined using a crude Monte Carlo sampling method⁴¹ where the electronic structure of points on the dividing surfaces was calculated “on the fly” using methods described in section 2.1. Typically, between 200 and 2000 samplings were needed for each dividing surface to obtain the chosen accuracy of 2% in the reactive flux through the dividing surface.

2.3. Classical Trajectory Simulations. The high-pressure limiting rate coefficient of reaction 1 was also obtained from classical trajectory (CT) simulations based on Keck's⁴³ procedure for initiating trajectories. An ensemble of trajectories was initiated at an approximate transition-state dividing surface and propagated forward and backward in time. The sampling was

done with statistical weights equal to the contribution to the reactive flux (within transition-state theory for the given dividing surface). With this approach,^{44–46} the high-pressure limiting rate coefficient is given by eq 6

$$k_{\infty}^{\text{CT}}(T) = \langle \chi_{\text{reac}}(q, p; S) \rangle k_{\infty}^{\text{TST}}(T; S) \quad (6)$$

where the reactivity factor (χ_{reac}) specifies whether the trajectory initiated at the phase space point (q, p) on the dividing surface S is reactive or not and k_{∞}^{TST} is the canonical rate coefficient. As previously,^{44–46} S was taken to be a canonically optimized dividing surface, and χ_{reac} was taken to be unity if the forward-propagated trajectories reached a certain minimum potential value (E_{min}) and the backward-propagated trajectories reached a fragment separation larger than a certain value (taken as 15 bohr) without reaching the minimum potential value. Otherwise, χ_{reac} was taken to be 0. The recrossing factor ($\langle \chi_{\text{reac}} \rangle$) was calculated for a set of E_{min} values, and if the recrossing factor reached a plateau value at low enough energies, the no-return condition was satisfied and the value of the recrossing factor was accepted. The zero-point vibrational energy of the O–H stretching mode was assumed to be constant over the whole PES investigated (see discussion in section 4).

2.4. Master Equation. The temperature and pressure dependence of the irreversible dissociation of H_2O_2 in an inert bath gas was studied using the two-dimensional master equation (2D-ME) given in eq 7

$$\frac{dn(E, J, t)}{dt} = Z \sum_{J'} \int_0^{\infty} P(E, J; E', J') n(E', J', t) dE' - Zn(E, J, t) - k(E, J) n(E, J, t) \quad (7)$$

Here, $n(E, J, t)dE$ is the number density of molecules with total energy between E and $E + dE$ and total angular momentum quantum number J at a given time t , Z is the collision rate of the molecule with the bath gas, $k(E, J)$ is the specific rate coefficient, and $P(E, J; E', J')$ is the probability of a molecule with energy between E' and $E' + dE'$ and total angular momentum quantum number J' being transferred by collision to a state with energy between E and $E + dE$ and total angular momentum quantum number J . The 2D-ME was reduced to an equivalent one-dimensional ME by using the E, J model of Miller et al.⁴⁷ In the E, J model the J distribution after a collision is assumed to be independent of the total angular momentum of the molecule before the collision. Thus, $P(E, J; E', J') = P(E, E')\phi(E, J)$; see Miller et al.⁴⁷ for a description of $\phi(E, J)$. The master equation was solved by methods described previously^{47–49} using the VARIFLEX program.⁵⁰

The energy-transfer function for the deactivating collisions was modeled using the “single-exponential down” expression (eq 8)

$$P(E, E') = \frac{1}{C_N(E')} \exp\left(-\frac{E' - E}{\langle \Delta E_d \rangle}\right) \quad E < E' \quad (8)$$

Here, C_N is a normalization constant, and ΔE_d is the average energy transferred by down transitions only.

The HOOH torsional mode was treated as a hindered internal rotor. The classical density of states of the torsional motion was obtained from eq 9

$$\rho_{\text{cl}}(E) = \frac{\sqrt{2I_r}}{h} \int H(E - V(\phi)) [E - V(\phi)]^{-1/2} d\phi \quad (9)$$

where $H(x)$ is the Heaviside step function and $V(\phi)$ is the potential for the torsional motion as a function of the dihedral angle ϕ .⁵¹ $V(\phi)$ was taken from Koput et al.¹⁸ (eq 10).

$$V(\phi)/\text{cm}^{-1} = 1037.4 \cos(\phi) + 647.2 \cos(2\phi) + 46.9 \cos(3\phi) + 2.7 \cos(4\phi) \quad (10)$$

This potential has a minimum at $\phi = 112.5^\circ$ with trans and cis barriers to internal rotation of 377 and 2545 cm^{-1} , respectively.¹⁸ The reduced moment of inertia (I_r) for the torsional motion was calculated using the method of Pitzer⁵² for unsymmetrical tops attached to a rigid frame, yielding $I_r = 7.04 \times 10^{-48} \text{ kg m}^2$. An estimate of the quantum density of states was obtained by applying a Pitzer–Gwinn-like⁵³ correction (eq 11)

$$\rho_q(E) = \rho_{\text{cl}}(E) \frac{\rho_q^{\text{ho}}(E)}{\rho_{\text{cl}}^{\text{ho}}(E)} \quad (11)$$

where $\rho_q^{\text{ho}}(E)$ and $\rho_{\text{cl}}^{\text{ho}}(E)$ are the quantum and classical harmonic oscillator densities of states, respectively.

The collision rate (Z) was assumed to be independent of energy and total angular momentum and was taken as the Lennard-Jones collision rate (Z_{LJ}). The following Lennard-Jones parameters were used:⁵⁴ $\sigma(\text{He}) = 2.610 \text{ \AA}$, $\sigma(\text{Ar}) = 3.350 \text{ \AA}$, $\sigma(\text{H}_2\text{O}_2) = 3.499 \text{ \AA}$, $\epsilon(\text{He}) = 7.23 \text{ cm}^{-1}$, $\epsilon(\text{Ar}) = 99.40 \text{ cm}^{-1}$, and $\epsilon(\text{H}_2\text{O}_2) = 255.85 \text{ cm}^{-1}$, where σ is the collision diameter and ϵ is the well depth.

In the master equation calculations, the value used for the HO–OH bond dissociation energy (at 0 K) was the experimental value measured by Luo et al.⁵⁵ The values used for rotational constants and vibrational frequencies of hydrogen peroxide and the hydroxyl radical were experimental values taken from the NIST Computational Chemistry Comparison and Benchmark Database.⁵⁶

3. Results

3.1. Potential Energy Surface. Equilibrium structural parameters of $\text{OH}(X^2\Pi)$ and $\text{H}_2\text{O}_2(X^1A)$ obtained in this work with the B3LYP, MP2, and CASPT2 models and the aug-cc-pVTZ basis set are compared to some previous calculated and experimental values in Table 1. Generally, the differences between calculated and measured parameters are within error margins reported from benchmark studies;^{27,57} however, the calculations predicted the HO–OH bond length (r_{OO}) to be between 1.0 and 2.5 pm shorter than that measured experimentally. The experimental HOOH dihedral angle reported in the NIST Computational Chemistry Comparison and Benchmark Database⁵⁶ and determined by Redington et al.⁵⁸ is larger than the value measured by Koput⁵⁹ and the calculated values.

Table 2 compares electronic (D_e) and bond (D_0) dissociation energies calculated in this work with some previously calculated and experimental values. If we look at the results obtained at the CCSD(T)/EB5Q//MP2/aug-cc-pVTZ level of theory, D_e is in excellent agreement with the value determined by Kuhn et al.,¹⁹ while the dissociation energy with anharmonic ZPE included is $\sim 0.7 \text{ kcal mol}^{-1}$ higher than that measured by Luo et al.⁵⁵ D_e and D_0 obtained at the CASPT2/aug-cc-pVTZ level are $\sim 3.4 \text{ kcal mol}^{-1}$ lower than the experimental values. There

TABLE 1: Equilibrium Structural Parameters of OH($X^2\Pi$) and H₂O₂(X^1A')^a

method	OH	H ₂ O ₂			
	<i>r</i>	<i>r</i> _{OH}	<i>r</i> _{OO}	∠ _{HOO}	τ _{HOOH}
B3LYP/aug-cc-pVTZ	0.975	0.967	1.451	100.7	113.3
MP2/aug-cc-pVTZ	0.970	0.967	1.454	99.6	112.6
CASPT2/aug-cc-pVTZ	0.971	0.966	1.468	99.4	113.3
experiment ^b	0.970	0.950	1.475	94.8	119.8
experiment ^c		0.965	1.464	99.4	111.8
analytical PES ^d		0.965	1.452	100.4	114.0
analytical PES ^e		0.962	1.450	100.0	112.6

^a Bond lengths (*r*) are given in Ångströms, and bond angles (∠) and torsional angles (τ) are given in degrees. ^b NIST Computational Chemistry Comparison and Benchmark Database.⁵⁶ ^c See Koput.⁵⁹ ^d See Kuhn et al.¹⁹ ^e See Koput et al.¹⁸

TABLE 2: Electronic (*D_e*) and Bond (*D₀*) Dissociation Energies (at 0 K) of the HO–OH Bond of H₂O₂(X^1A')

method ^a	<i>D_e</i> /kcal mol ^{−1}	<i>D₀</i> /kcal mol ^{−1}	
		harmonic	anharmonic
B3LYP/aTZ	50.7	44.7	
MP2/aTZ	59.8	54.0	54.8
CCSD(T)/aTZ//MP2/aTZ	52.2	46.4	47.1
CCSD(T)/aQZ//MP2/aTZ	53.5	47.8	48.5
CCSD(T)/a5Z//MP2/aTZ	54.0	48.2	48.9
CCSD(T)/EBQT//MP2/aTZ	54.5	48.8	49.5
CCSD(T)/EB5Q//MP2/aTZ	54.4	48.7	49.4
CASPT2/aTZ	51.2	45.4	
CASPT2/ANO ^b	51.6		
MRSDCI/cc-pVTZ ^b	52.7		
experiment ^b	54.5		
experiment ^c		48.753 ± 0.010	

^a Abbreviations: aXZ = aug-cc-pVXZ; EBXY = basis set extrapolation of aug-cc-pVXZ and aug-cc-pVYZ where *Y* = *X* − 1; see eq 4. ^b See Kuhn et al.¹⁹ ^c See Luo et al.⁵⁵

is good agreement between our CASPT2/aug-cc-pVTZ calculation and the CASPT2/ANO calculation by Kuhn et al.;¹⁹ the MRSDCI/cc-pVTZ calculation by Kuhn and co-workers gives slightly better agreement with experiment.

At infinite separation, the 16 potential energy hypersurfaces of the 2 OH radicals converge to 3 surfaces separated in energy by an energy gap corresponding to the spin–orbit interaction parameter, $|A| = 138.68$ cm,⁶⁰ and with the electronic statistical weights 4 ($^2\Pi_{3/2} + ^2\Pi_{3/2}$), 8 ($^2\Pi_{3/2} + ^2\Pi_{1/2}$), and 4 ($^2\Pi_{1/2} + ^2\Pi_{1/2}$).²² Harding¹⁷ found that when $r_{OO} > 8$ Å, the interaction potential is mainly a dipole–dipole interaction, while at intermediate distances, hydrogen bonding is the dominant attractive force. At $r_{OO} < 2.5$ Å, the interaction is characterized by a covalent bonding forces, and only one PES is attractive. Further, Harding¹⁷ found that two equivalent hydrogen-bonded OH dimers exist on the two lowest singlet surfaces and a transition state connects one of the dimers and hydrogen peroxide.

Our calculations confirm the findings of Harding.¹⁷ Displayed in Figures 1 and 2 are the structures of one of the hydrogen-bonded OH dimers (X^1A' in *C_s* symmetry) and the X^1A' transition state (TS1) connecting the two equivalent hydrogen-bonded OH dimers, respectively. If we start by looking at Figure 2, our calculations at the CASPT2/aug-cc-pVDZ and CASPT2/aug-cc-pVTZ levels of theory predict essentially the same TS structure as Harding's¹⁷ CAS+1+2/cc-pVDZ calculation. The two OH radicals are, however, slightly more separated (~2.5 pm) at the CASPT2/aug-cc-pVDZ level. When it comes to the H-bonded OH dimer, we see in Figure 1 that Harding¹⁷ predicted the dimer to have *C_s* symmetry, while we predict the dimer to

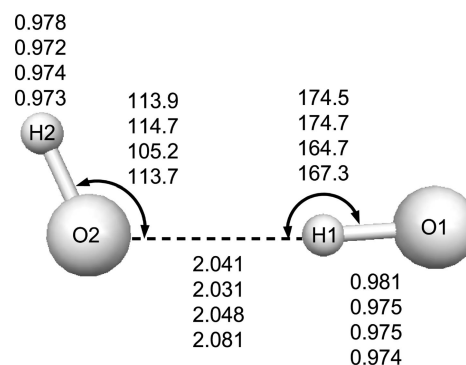


Figure 1. Structure of the hydrogen-bonded OH dimer as calculated by the CASPT2/aug-cc-pVDZ (this work; top row values), CASPT2/aug-cc-pVTZ (this work; second row values), CAS+1+2/cc-pVDZ (this work; third row values), and CAS+1+2/cc-pVDZ (Harding;¹⁷ bottom row values) models. Bond lengths are given in Ångströms, and bond angles are given in degrees. The dihedral angle is $\tau_{H2-O2-O1-H1} = 129.4$ and 130.0° at the CASPT2/aug-cc-pVDZ and CASPT2/aug-cc-pVTZ levels of theory, respectively. Note, however, that the CAS+1+2/cc-pVDZ model both in this work and in the work of Harding¹⁷ predicted the dimer to have *C_s* symmetry.

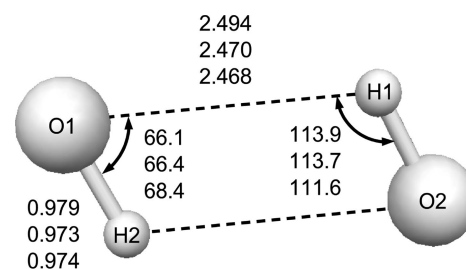


Figure 2. Structure of X^1A' transition state connecting two equivalent hydrogen-bonded OH dimers as calculated by the CASPT2/aug-cc-pVDZ (this work; top row values), CASPT2/aug-cc-pVTZ (this work; second row values), and CAS+1+2/cc-pVDZ (Harding;¹⁷ bottom row values) models. Bond lengths are given in Ångströms, and bond angles are given in degrees.

TABLE 3: Electronic Energy of Stationary Points on the Ground-State Potential Energy Hypersurface of the Reaction OH + OH → H₂O₂ Relative to the Energy of the Reactants

stationary point	energy/kcal mol ^{−1}		
	CASPT2/ aug-cc-pVDZ	CASPT2/ aug-cc-pVTZ	CAS+1+2/ aug-cc-pVDZ ^a
H-bonded OH dimer ^b	−3.89	−3.89	−4.25
TS1 ^c	−2.94	−2.89	−3.49
TS2 ^d	−3.53	−3.53	−3.35

^a See Harding.¹⁷ ^b Figure 1. ^c Figure 2. ^d Figure 3.

have no symmetry. The HOOH dihedral angle is predicted to be 129.4 and 130.0° at the CASPT2/aug-cc-pVDZ and CASPT2/aug-cc-pVTZ levels of theory, respectively. To investigate this issue further, we have carried out additional calculations at the CAS+1+2/cc-pVDZ level of theory with the MOLPRO program²⁸ using the same active space as that used in the CASPT2 calculations. The results are included in Figure 1, and in short, our CAS+1+2/cc-pVDZ calculation also predicted the OH dimer to have *C_s* symmetry. Adding diffuse functions to the basis set (aug-cc-pVDZ) did not change the situation. The calculated electronic energies of the OH dimer and TS1 are given in Table 3. The difference between the CASPT2/aug-cc-pVDZ and CASPT2/aug-cc-pVTZ levels of theory is at most 0.05 kcal mol^{−1}. The energies reported by Harding¹⁷ at the CAS+1+2/cc-pVDZ level are lower than those predicted in this work.

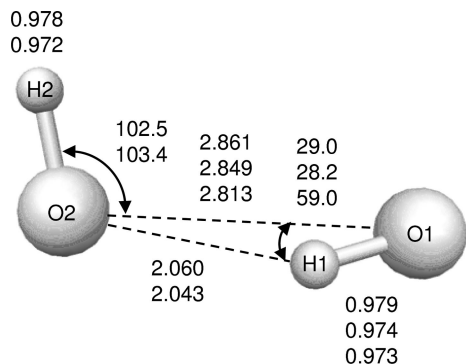


Figure 3. Structure of the transition state connecting hydrogen peroxide and the hydrogen-bonded OH dimer shown in Figure 1, as calculated by the CASPT2/aug-cc-pVDZ (top row values) and CASPT2/aug-cc-pVTZ (second row values) models. The dihedral angle is $\tau_{\text{H2-O2-O1-H1}} = 118.1$ and 118.8° at the CASPT2/aug-cc-pVDZ and CASPT2/aug-cc-pVTZ levels of theory, respectively. The third row values are the parameters calculated by Harding¹⁷ at the CAS+1+2/cc-pVDZ level of theory. Harding also reported $\tau_{\text{H2-O2-O1-H1}} = 143^\circ$. Bond lengths are given in ångströms, and bond angles are given in degrees.

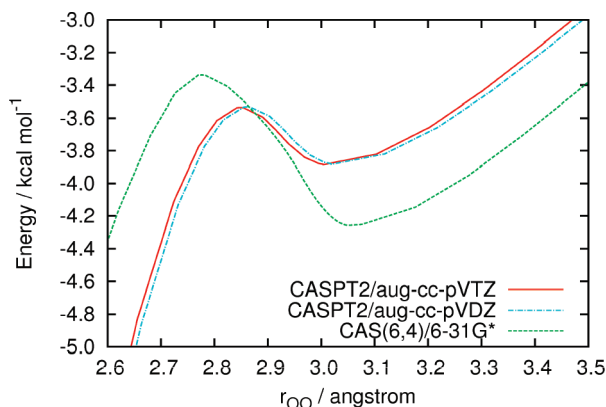


Figure 4. Minimum-energy path for the reaction $\text{OH} + \text{OH} \rightarrow \text{H}_2\text{O}_2$ (X^1A) as a function of the HO-OH bond length (r_{OO}).

Figure 3 displays the structure of the transition state (TS2) connecting hydrogen peroxide and the H-bonded OH dimer shown in Figure 1. As can be seen, the TS structure becomes slightly tighter when the basis set is enlarged. Harding¹⁷ predicted a tighter TS structure, which might be attributed to the lack of diffuse functions in the basis set employed by Harding. Both the CASPT2/aug-cc-pVDZ model and the CASPT2/aug-cc-pVTZ model predicted the electronic energy of TS2 to be $-3.53 \text{ kcal mol}^{-1}$, while Harding,¹⁷ on the other hand, reported $-3.35 \text{ kcal mol}^{-1}$ (see Table 3).

The minimum-energy path (MEP) connecting TS2 and the OH dimer is displayed in Figure 4 as function of r_{OO} . For the CASPT2 model, we see that the potential becomes less attractive when the basis set is enlarged. In the region of $2.5 < r_{\text{OO}} < 5.0 \text{ Å}$, the difference between the CASPT2/aug-cc-pVDZ and CASPT2/aug-cc-pVTZ methods is, at most, $0.3 \text{ kcal mol}^{-1}$.

3.2. High-Pressure Limit. The MEP of reaction 1, displayed in Figure 4, is characterized by a barrier below the energy of the reactants and the presence of a hydrogen-bonded adduct. Similar reaction systems have recently been interpreted in terms of a two-transition-state model (2TS).^{61–63} In this model, it is assumed that the hydrogen-bonded complex has so short of a lifetime that it does not undergo any collisions. Further, it is anticipated that at relatively high temperatures, the reaction rate is controlled by an “inner” transition state located in the vicinity of the barrier and by an “outer” transition state at low

temperatures. Following Greenwald et al.,⁶² the effective flux through both transition states can be approximated by eq 12

$$N_{\text{eff}}^\ddagger(E, J) = \frac{N_{\text{inner}}^\ddagger(E, J)N_{\text{outer}}^\ddagger(E, J)}{N_{\text{inner}}^\ddagger(E, J) + N_{\text{outer}}^\ddagger(E, J)} \quad (12)$$

where $N_{\text{inner}}^\ddagger$ and $N_{\text{outer}}^\ddagger$ are the E - and J -resolved number of states at the inner and outer transition states, respectively.

In this work, we have tested three different methods for handling this situation, namely, E , J -resolved VRC-TST (section 2.2), classical trajectory simulations (section 2.3), and the above-mentioned 2TS model. In our trajectory simulations, the PES is evaluated “on the fly”. Thus, in order for the trajectory simulations to be computationally feasible, analytical gradients must be available for the selected electronic structure method. We therefore chose to evaluate the potential at the CAS(6,4)/6-31G* level of theory. As seen in Figure 4, CAS(6,4)/6-31G* gives a qualitatively correct description of the important parts of the PES compared to the CASPT2 calculations. The trajectory simulations were performed for seven different dividing surfaces, covering the temperature range of 200–2100 K. Thus, both the inner and the outer transition states were described. However, because of the computational cost, only 200 trajectories for each dividing surface were sampled. This gives an error in the recrossing factor of 7%. The sampling error in the rate coefficient obtained from canonical VRC-TST was 2%. Therefore, the error in the rate coefficient from the trajectory simulations (eq 6) is mainly given by the error in the recrossing factor.

As mentioned in section 2.2, dividing surfaces are defined in terms of a fixed distance between pivot points on each fragment within VRC-TST. In the E , J -resolved VRC-TST calculations, the pivot points were located on each oxygen nucleus with pivot point to pivot point separations ranging from 4.5 to 11.0 bohr with a grid spacing of 0.5 bohr. To make the calculations comparable with the trajectory calculations, the PES was evaluated at the CAS(6,4)/6-31G* level of theory for this case also.

When it comes to the 2TS model, both $N_{\text{inner}}^\ddagger$ and $N_{\text{outer}}^\ddagger$ were obtained from E , J -resolved VRC-TST calculations. Dividing surfaces for the “inner” transition state were defined by locating the pivot points on each oxygen nuclei with pivot point to pivot point separations ranging from 4.5 to 5.5 bohr with a grid spacing of 0.1 bohr. The dividing surfaces for the “outer” transition state were defined by locating the pivot points on each oxygen nuclei with pivot point to pivot point separations in the range of 6.5–11.0 bohr with a grid spacing of 0.5 bohr. Qualitatively, two factors control which dividing surface provides the lowest estimate for the number of states. One can be called an entropic factor and is related to the area of the dividing surface which makes an effective contribution to the number of states, and the other is the energy factor which depends on the minimal energy configuration on the dividing surface. The inner transition state, which is more contracted than the outer one, provides a dynamical bottleneck at higher energies where the entropic factor is the most important one. At lower energies where the energy factor becomes a dominating one, the outer transition state provides a smaller estimate for the number of states. No dividing surfaces were placed in the region where the hydrogen-bonded complex is located because, both entropically and energetically, these dividing surfaces would make larger contributions to $N_{\text{eff}}^\ddagger(E, J)$ than the inner transition state for any values of E and J . Again, the PES was

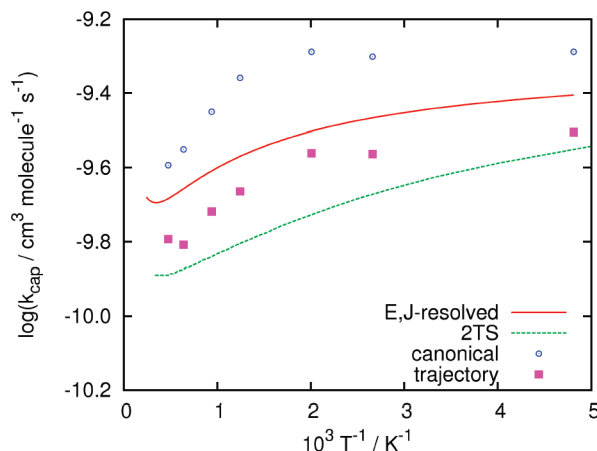


Figure 5. Capture rate coefficient (k_{cap}) for the reaction $\text{OH} + \text{OH} \rightarrow \text{H}_2\text{O}_2$ (X^1A) as obtained from E , J -resolved variable reaction coordinate transition-state theory (VRC-TST), canonical VRC-TST, classical trajectory simulations, and a two-transition-state model (2TS); see text for details. The potential energy hypersurface was calculated at the CAS(6,4)/6-31G* level of theory.

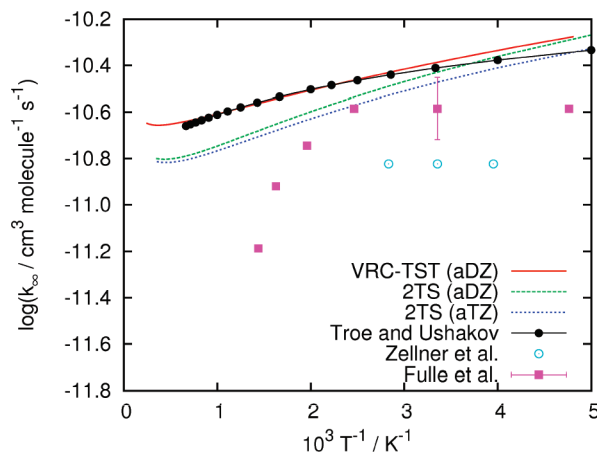


Figure 6. High-pressure limiting rate coefficient (k_{∞}) for the reaction $\text{OH} + \text{OH} \rightarrow \text{H}_2\text{O}_2$ (X^1A) as obtained from E , J -resolved variable reaction coordinate transition-state theory (VRC-TST) and a two-transition-state model (2TS), compared to the experimental results of Zellner et al.¹¹ and Fulle et al.¹³ and the SACM/CT calculation of Troe and Ushakov.²³ The potential energy hypersurface of the reaction was obtained using the CASPT2 model with the aug-cc-pVDZ (aDZ) and aug-cc-pVTZ (aTZ) basis sets.

evaluated at the CAS(6,4)/6-31G* level of theory. The effective number of states of the TS was obtained from eq 12 and inserted into eq 5 to obtain the high-pressure limiting rate coefficient.

Figure 5 displays the capture rate coefficient ($k_{\text{cap}} = k_{\infty}/f_{\text{el}}$) as obtained from the trajectory simulations, canonical VRC-TST, E , J -resolved VRC-TST, and the 2TS model. Although only a small number of trajectories were sampled, the agreement between the E , J -resolved VRC-TST calculations and the trajectory simulations is remarkably good. The difference between k_{cap} obtained from the E , J -resolved VRC-TST calculations and k_{cap} obtained from the trajectory simulations varied between 0.71 and 0.87 for the different temperatures investigated. Given the small number of trajectories sampled, an average equal to 0.8 is taken as the dynamical correction factor. This correction is very similar to what has previously been found for the $\text{CH}_3 + \text{CH}_3$ reaction system.⁶⁴ We see also in Figure 5 that the trajectory simulations and the 2TS model predict similar rates at temperatures below 300 K and above 1500 K. At intermediate temperatures, however, the 2TS model predicts

smaller capture rates than the trajectory simulations and the E , J -resolved VRC-TST calculations. On the basis of these results and the above-mentioned theoretical considerations, we conclude that the 2TS model provides the best theoretical description of the high-pressure limiting rate coefficient of reaction 1.

Figure 6 shows the high-pressure limiting rate coefficient of reaction 1 as calculated with E , J -resolved VRC-TST and the 2TS model. The high-pressure limiting rate coefficient obtained with E , J -resolved VRC-TST includes the dynamical correction factor of 0.8 (see above), and the PES was calculated at the CASPT2/aug-cc-pVDZ level of theory. For the 2TS model, on the other hand, the potential energy hypersurface of the reaction was calculated both at the CASPT2/aug-cc-pVDZ and the CASPT2/aug-cc-pVTZ levels of theory. The factor f_{el} was taken as

$$f_{\text{el}} = \frac{Q_{\text{el}}(\text{H}_2\text{O}_2)}{Q_{\text{el}}(\text{OH})Q_{\text{el}}(\text{OH})} = \frac{1}{4 + 8 \exp(-E_{\text{SO}}/k_{\text{B}}T) + 4 \exp(-2E_{\text{SO}}/k_{\text{B}}T)} \quad (13)$$

where $E_{\text{SO}} = 138.68 \text{ cm}^{-1}$ is the energy splitting between the spin-orbit states.⁶⁰ We see in Figure 6 that VRC-TST and the two 2TS models predict quite similar values for the rate coefficient at low temperatures, but the 2TS models predict smaller values when the temperature is increased (around 40% at 3000 K). Thus, the bottleneck in the flux through the outer-transition-state region still contributes to the overall rate at this temperature. The 2TS model employing the CASPT2/aug-cc-pVTZ PES gives slightly smaller rate coefficients at low temperatures than the 2TS model, where the potential was obtained with the aug-cc-pVDZ basis set (~15% at 200 K). The results obtained with the 2TS model and the CASPT2/aug-cc-pVTZ PES could be fitted to the following expression in units of $\text{cm}^3 \text{ molecule}^{-1} \text{ s}^{-1}$

$$k_{1,\infty}(T) = 9.3 \times 10^{-9} T^{-1.040} \exp(3.5/T) + 1.13 \times 10^{-12} T^{0.303} \exp(84/T) \quad (14)$$

We see in Figure 6 that the values for the high-pressure limiting rate coefficient calculated in this work are larger than the values reported by Zellner et al.¹¹ and Fulle et al.¹³ obtained on the basis of extrapolation of experimental falloff curves. Zellner and co-workers reported $1.5 \times 10^{-11} \text{ cm}^3 \text{ molecule}^{-1} \text{ s}^{-1}$ over the temperature range of 253–353 K. At 298 K, Fulle and co-workers reported $k_{\infty} = 2.6 \times 10^{-11} \text{ cm}^3 \text{ molecule}^{-1} \text{ s}^{-1}$, whereas $3.4 \times 10^{-11} \text{ cm}^3 \text{ molecule}^{-1} \text{ s}^{-1}$ was obtained in this work with the 2TS model employing the CASPT2/aug-cc-pVTZ PES. If we compare our values to the values calculated by Troe and Ushakov²³ using SACM/CT, there is generally very good agreement between the different models. At 298 K, Troe and Ushakov reported $3.9 \times 10^{-11} \text{ cm}^3 \text{ molecule}^{-1} \text{ s}^{-1}$, in excellent agreement with our value obtained with the 2TS model employing the CASPT2/aug-cc-pVTZ PES. For higher temperatures, the 2TS model predicts smaller rate coefficients than the SACM/CT model. At 1500 K, we report $1.6 \times 10^{-11} \text{ cm}^3 \text{ molecule}^{-1} \text{ s}^{-1}$, whereas $2.2 \times 10^{-11} \text{ cm}^3 \text{ molecule}^{-1} \text{ s}^{-1}$ was reported by Troe and Ushakov.²³ In a study of the secondary kinetics of methanol decomposition, Jasper et al.⁶⁵ also calculated $k_{1,\infty}$ using VRC-TST and found excellent agreement with the results reported by Troe and Ushakov.

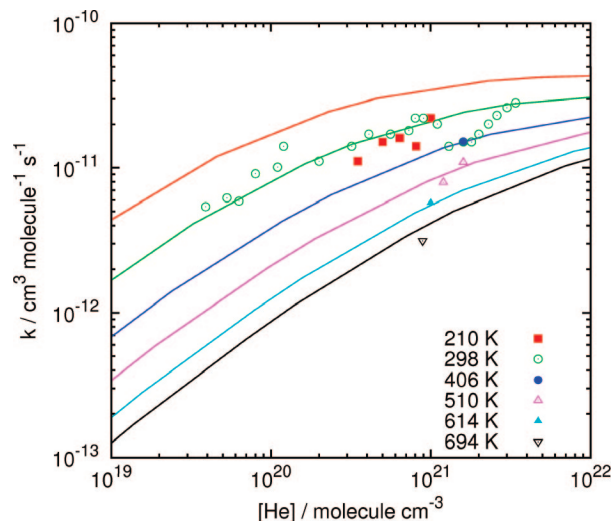


Figure 7. Falloff curves for the reaction $\text{OH} + \text{OH} + \text{He} \rightarrow \text{H}_2\text{O}_2 + \text{He}$ as calculated using a two-dimensional master equation (eq 7). The scatter points are the experimental data of Forster et al.¹² (298 K) and Fulle et al.¹³

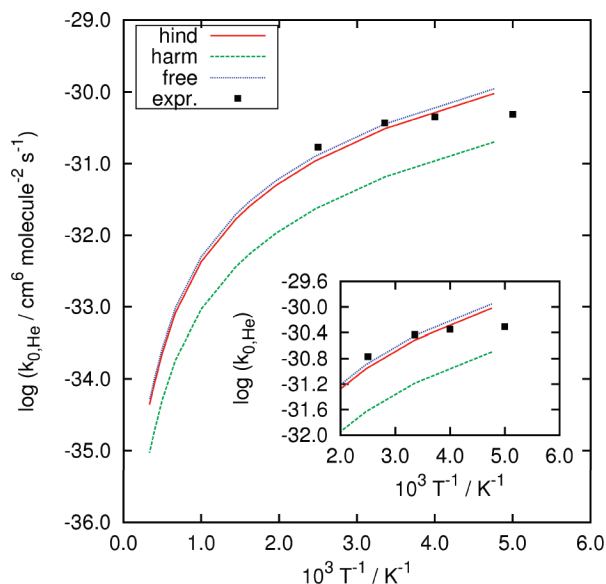


Figure 8. Low-pressure limiting rate coefficient (k_0) as function of temperature (T) for the reaction $\text{OH} + \text{OH} + \text{He} \rightarrow \text{H}_2\text{O}_2 + \text{He}$ as calculated using a two-dimensional master equation (eq 7) where the HOOH torsional mode has been treated either as a harmonic oscillator, hindered rotor, or free rotor. The scatter points are the experimental data of Forster et al.¹² (298 K) and Fulle et al.¹³ The inset shows the same data but for the temperature range of 200–500 K.

3.3. Falloff Behavior and Low-Pressure Limit. The pressure dependence of reaction 1 was analyzed using the two-dimensional master equation (2D-ME) given by eq 7. Figures 7 and 8 show the pressure dependence and the low-pressure limiting rate coefficient, respectively, of reaction 1 with He as the bath gas for several temperatures. The falloff curves and k_0 were obtained by adjusting the value of $\langle \Delta E_d \rangle$ to give best possible agreement with the experimental data of Forster et al.¹² and Fulle et al.¹³ This was obtained by taking $\langle \Delta E_d \rangle = 200(T/298 \text{ K})^{0.1} \text{ cm}^{-1}$. Over the temperature range of 200–3000 K, our data could be fitted to the following low-pressure limiting rate coefficient in units of $\text{cm}^6 \text{ molecule}^{-2} \text{ s}^{-1}$

$$k_{1,0}(\text{M} = \text{He}) = 4.4 \times 10^{-20} T^{-4.30} \exp(-340/T) \quad (15)$$

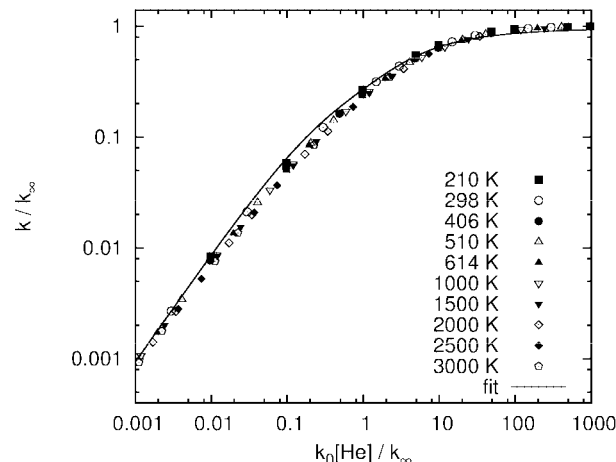


Figure 9. Doubly reduced falloff curve for the reaction $\text{OH} + \text{OH} + \text{He} \rightarrow \text{H}_2\text{O}_2 + \text{He}$ as calculated using a two-dimensional master equation (scatter points). Fit of the data to eq 16 gave a center broadening factor of $F_{\text{cent}} = 0.54 \pm 0.01$ (the error corresponds to 1σ from the statistical analysis).

In Figure 9, our rate data are presented as a doubly reduced falloff curve. The falloff behavior was described by the symmetric expression

$$\frac{k}{k_{\infty}} = \left(\frac{x}{1+x} \right) F_{\text{cent}}^{1/[1+(\log x/N)^2]} \quad (16)$$

where $x = k_0[\text{M}]/k_{\infty}$, $N \approx 0.75 - \log F_{\text{cent}}$, and F_{cent} is the center broadening factor.¹⁵ Under the assumption that F_{cent} is independent of temperature, fit of the data in Figure 9 to eq 16 gave $F_{\text{cent}} = 0.54 \pm 0.01$ (1σ) over the temperature range of 200–3000 K. Generally, our calculations provide a very good description of the experimental data of Forster et al.¹² and Fulle et al.¹³ for temperatures between 298 and 694 K. However, our 2D-ME calculations cannot explain the observations at 210 K.

For reaction 1 with argon as the bath gas, we have analyzed the experimental data of Kappel et al.¹⁴ Kappel and co-workers investigated the dissociation of hydrogen peroxide at pressures of about 1, 4, and 15 bar over the temperature range of 950–1250 K. The results from our 2D-ME calculations are shown in Figure 10. The falloff curves were obtained by taking $\langle \Delta E_d \rangle = 300(T/298 \text{ K})^{0.5} \text{ cm}^{-1}$, which is identical to the expression used for the $\text{H} + \text{OH} + \text{Ar} \rightarrow \text{H}_2\text{O} + \text{Ar}$ reaction.⁶⁶ As seen in Figure 10, there is at 950 K excellent agreement between our values obtained with the 2D-ME and the experimental values of Kappel et al.¹⁴ However, as the temperature is increased, the agreement becomes worse. The experimental data seem to systematically fall off faster from the low-pressure limit than can be explained by our 2D-ME calculations. Turning to the low-pressure limiting rate coefficient, there is again excellent agreement between our value and the value measured by Kappel and colleagues, although the temperature dependence of $k_{-1,0}$ is slightly different (see Figure 11). Over the temperature range of 500–3000 K, we report

$$k_{-1,0}(\text{M} = \text{Ar}) = 1.4 \times 10^8 T^{-4.57} \exp(-26322/T) \text{ cm}^3 \text{ molecule}^{-1} \text{ s}^{-1} \quad (17)$$

Figure 12 shows the doubly reduced falloff curve for the dissociation of hydrogen peroxide with Ar as the bath gas. Fit

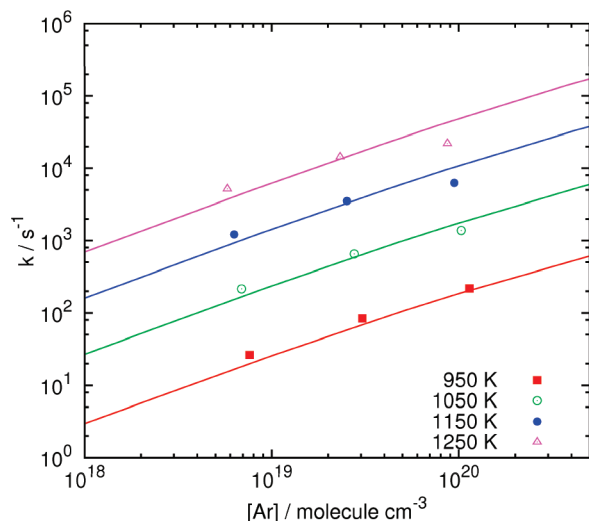


Figure 10. Falloff curves for the reaction $\text{H}_2\text{O}_2 + \text{Ar} \rightarrow \text{OH} + \text{OH} + \text{Ar}$ as calculated using a two-dimensional master equation (eq 7). The scatter points are the experimental data of Kappel et al.¹⁴

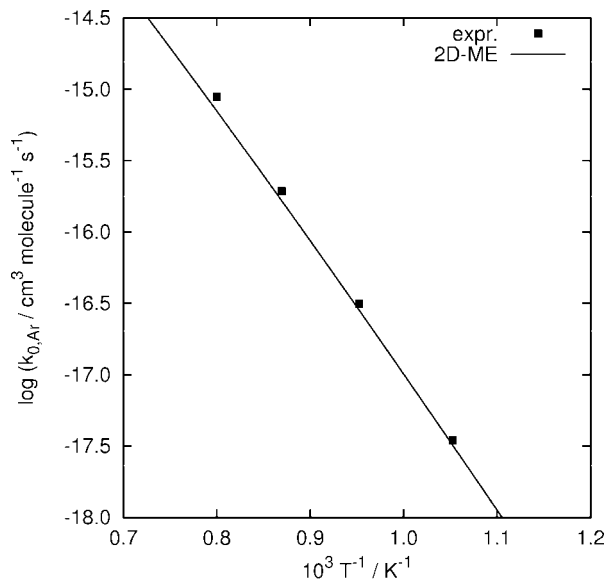


Figure 11. Low-pressure limiting rate coefficient (k_0) as function of temperature (T) for the reaction $\text{H}_2\text{O}_2 + \text{Ar} \rightarrow \text{OH} + \text{OH} + \text{Ar}$ as calculated using a two-dimensional master equation (eq 7). The scatter points are the experimental data of Kappel et al.¹⁴

of the data to eq 16 gave $F_{\text{cent}} = 0.55 \pm 0.01$ (1σ) over the temperature range of 500–3000 K.

4. Discussion

As already mentioned, there is generally good agreement between the different models for computing the high-pressure limiting rate coefficient of reaction 1. There are, however, some differences. If we start by comparing our E , J -resolved VRC-TST model to the SACM/CT model employed by Troe and Ushakov,²³ we see in Figure 6 that the two models only differ at low temperatures. In our VRC-TST calculations, we have taken the O–O bond (r_{OO}) as the reaction coordinate. This is likely a good reaction coordinate for high temperatures but not necessarily for low temperatures. We have tested this by locating the pivot points at the center of mass of each OH radical. Our VRC-TST calculations for the two cases predicted essentially similar rate coefficients for temperatures less than 600 K. Most likely, the discrepancy at low temperatures can be attributed to

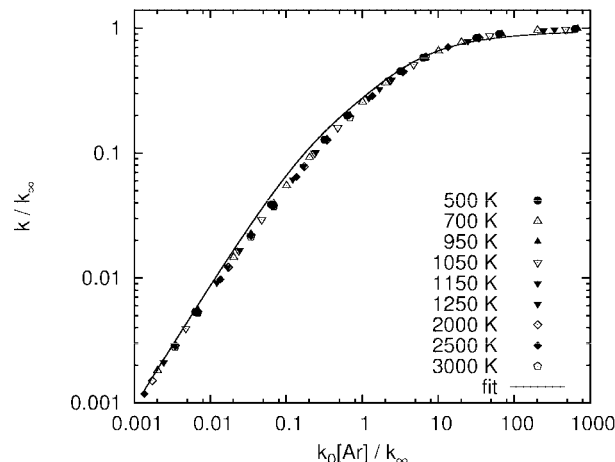


Figure 12. Doubly reduced falloff curve for the reaction $\text{H}_2\text{O}_2 + \text{Ar} \rightarrow \text{OH} + \text{OH} + \text{Ar}$ as calculated using a two-dimensional master equation (scatter points). Fit of the data to eq 16 gave a center broadening factor of $F_{\text{cent}} = 0.55 \pm 0.01$ (the error corresponds to 1σ from the statistical analysis).

the rather small basis set employed in the E , J -resolved VRC-TST calculations. This is clearly seen for the 2TS model where the PES has been obtained both at the CASPT2/aug-cc-pVDZ and the CASPT2/aug-cc-pVTZ levels of theory. When the aug-cc-pVDZ basis set is employed, the 2TS model predicts a similar value for $k_{1,\infty}$ as the VRC-TST model. When the basis set is enlarged, the 2TS model and the SACM/CT model predict nearly identical rates. We attribute the difference between the 2TS model and the SACM/CT model for higher temperatures to the smaller effective number of states ($N_{\text{eff}}^{\ddagger}(E, J)$) predicted by the 2TS model.

One issue regarding the VRC-TST model that is important to keep in mind is that the model relies on the separation of transitional and conserved degrees of freedom. We have assumed that the O–H vibrational stretching mode ($\tilde{\nu}_{\text{OH}}$) could be treated as a conserved mode. We have not backed up this assumption with calculations but relied on our previous work on the $\text{H} + \text{O}_2 \rightarrow \text{HO}_2$ and $\text{H} + \text{OH} \rightarrow \text{H}_2\text{O}$ reactions.⁶⁶ If we look at the $\text{H} + \text{OH}$ reaction system, the MEP was calculated with relaxed and constrained O–H bond lengths. It was found that the contribution from the conserved $\tilde{\nu}_{\text{OH}}$ mode nearly canceled over the whole region of the MEP investigated. The same conclusion was found for the $\text{H} + \text{O}_2$ reaction system. Also, when we look at the O–H bond length (r_{OH}) for the stationary points on the PES of reaction 1, the variation in r_{OH} is, at most, 1 pm at the CASPT2/aug-cc-pVTZ level of theory, ranging from 0.975 Å for the OH dimer (Figure 1) to 0.966 Å for H_2O_2 (Table 1). It therefore seems reasonable to assume that $\tilde{\nu}_{\text{OH}}$ can be treated as a conserved mode for the $\text{OH} + \text{OH}$ reaction system. The same argument is used for justifying the treatment of $\tilde{\nu}_{\text{OH}}$ as a conserved mode in the classical trajectory simulations.

In the calculation of the high-pressure limiting rate coefficient of reaction 1, we have not included the orientation-dependent effect of spin–orbit coupling but relied on our previous work on the $\text{H} + \text{OH} \rightarrow \text{H}_2\text{O}$ reaction.⁶⁶ In this work, we found that shifting the energy of the reactants to the lowest spin–orbit state and taking $2 + 2 \exp(-E_{\text{SO}}/k_{\text{B}}T)$ as the electronic partition function for the OH radical provided a good approximation to the calculation where the orientation-dependent spin–orbit coupling was included ($E_{\text{SO}} = 138.68 \text{ cm}^{-1}$). The approximated treatment of the spin–orbit interaction gave slightly larger values for the rate coefficient, but the difference was less than 10%,

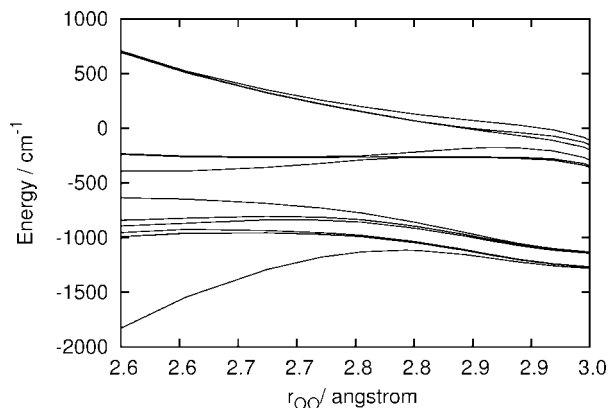


Figure 13. Spin-orbit coupling along the minimum-energy path for the reaction $\text{OH} + \text{OH} \rightarrow \text{H}_2\text{O}_2$ (X^1A) in the region near the transition state displayed in Figure 3.

and the effect was largest for the lowest temperatures. This is similar to what other researchers have found.^{65,67} Thus, it is reasonable to assume that this approximation can be used for the $\text{OH} + \text{OH}$ reaction system also. Unpublished calculations by Jasper and Klippenstein on reaction 1 support this assumption.⁶⁸

Another approximation made in the calculations was to neglect the angular momentum coupling of the electronic and rotational degrees of freedom in the OH radical. This rovibronic coupling is expected to be most important at low temperatures and may contribute significantly to the total partition function of OH. As argued by Jasper and co-workers,^{65,67} this approximation may be justified in the high-pressure limit for association reactions if the contribution of the rovibronic coupling to the reactive flux at the transition state is comparable to its asymptotic contribution. We investigated this further by calculating the spin-orbit coupling along the minimum-energy path of reaction 1 in the region near the saddle point shown in Figure 3. The spin-orbit matrix elements were computed using the Breit-Pauli operator where wave functions for the spin-orbit states were generated using multireference configuration interaction with CASSCF reference configurations only and the 6-311++G(3df,p) basis set (MOLPRO²⁸ was used in the calculations). The results from the calculations are displayed in Figure 13. At $r_{\text{OO}} \sim 3$ Å, the four lowest spin-orbit states are nearly degenerate, split by 12–15 cm^{-1} . The next four spin-orbit states are also nearly degenerate and lies 138–150 cm^{-1} above the lowest state. Thus, there is still significant spin-orbit coupling present at this fragment separation. First, at the saddle point, the degeneracy is significantly lifted. Thus, it seems plausible to assume that the effect of rovibronic coupling is of similar magnitude for the transition-state species and the reactants at large fragment separations. Since we neglect rovibronic coupling when computing $N^\ddagger(E, J)$, we also neglect it for the reactants and use the classical electronic partition function for OH. As the temperature is increased, the electronic motion and the nuclear rotation will uncouple.⁶⁹ Jasper et al.⁶⁷ have estimated that the coupled and uncoupled electronic-rotational partition functions for OH differ by less than 5% at 1000 K. It therefore seems safe to neglect the effect of rovibronic coupling for higher temperatures also. The cancellation of the effects of rovibronic coupling will not occur when calculating rate coefficients for the dissociation reaction because then, the reactant partition function is that of the complex. However, since the dissociation reaction is only of interest for high temperatures, we have neglected the contribution from rovibronic coupling for this situation also.

If we turn to the pressure dependence of reaction 1 with helium as the bath gas, our calculations provide a good description of the experimental data for temperatures between 298 and 694 K (Figure 7). We see, however, that the experimental rate coefficients at 210 and 298 K are indistinguishable within the reported uncertainty. This is not supported by our 2D-ME calculations. It should be noted that it is far from trivial to measure the rate coefficient for this reaction. In the experiment, there is competition between reactions 1 and 3, and the measured rate coefficient is actually a sum of k_1 and k_3 . There are a number of measurements of k_3 at room temperature, and they fall in the range of $(1.4\text{--}2.3) \times 10^{-12} \text{ cm}^3 \text{ molecule}^{-1} \text{ s}^{-1}$.⁷⁰ Both Forster et al.¹² and Fulle et al.¹³ used $1.9 \times 10^{-12} \text{ cm}^3 \text{ molecule}^{-1} \text{ s}^{-1}$ for k_3 , which was the previous IUPAC preferred value. Recent studies, however, report values for $k_3(298 \text{ K})$ near $1.4 \times 10^{-12} \text{ cm}^3 \text{ molecule}^{-1} \text{ s}^{-1}$.⁷⁰ According to Fulle and co-workers, the determination of k_1 is less sensitive to the value of k_3 at temperatures below 400 K but becomes very sensitive for higher temperatures, suggesting that the explanation for the discrepancy at 210 K must be sought elsewhere. One may speculate that the discrepancy is due to the neglect of the angular momentum coupling of the electronic and rotational degrees of freedom in the OH radical discussed above. Inclusion of this rovibronic coupling may explain some of the differences but hardly all. According to Jasper and Klippenstein,⁶⁸ the ratio between the uncoupled and coupled electronic-rotational partition functions for OH is 0.8 at 210 K. Presently, we can therefore offer no explanation for this discrepancy. The experiments by Fulle et al.¹³ at 210 K were carried out at high pressures. To resolve the apparent discrepancy, experimental data at low pressures would be of value. Future theoretical studies should investigate the effect of rovibronic coupling in more detail.

As already seen in Figure 8, there is at room temperature excellent agreement between our value for $k_{1,0}(\text{M} = \text{He})$ and the value measured by Fulle et al.¹³ However, the temperature dependence of $k_{1,0}(\text{M} = \text{He})$ below 250 K reported by Fulle and co-workers is much weaker than what we calculated with the 2D-ME. We attribute this discrepancy to the fact that the experimental $k_{1,0}(\text{M} = \text{He})$ was based on the value at 298 K measured by Forster et al.,¹² and its temperature dependence was obtained from rather simple calculations.^{15,20}

The calculated falloff curves for reaction 1 with He and Ar as the bath gases are not fully described by the symmetric expression given by eq 16 (see Figure 9). As also suggested by Troe and Ushakov,²³ the falloff behavior of this reaction should rather be described by an asymmetric expression. However, for combustion modeling purposes, the symmetric expression provides a convenient and sufficiently accurate description of the falloff behavior.

Regarding the experimental data of Trainor and von Rosenberg¹⁰ and Zellner et al.¹¹ for reaction 1 with N_2 as the bath gas, there is an apparent factor of 2.7 difference between the two measurements at room temperature. As shown by Forster et al.,¹² k_1 and k_3 can only be distinguished unambiguously when a large part of the falloff curve is analyzed, and when this is done, the measurements of Trainor and von Rosenberg and Zellner et al. are consistent. Until new experimental data with N_2 as the bath gas become available, it appears more reasonable to obtain $k_{1,0}(\text{M} = \text{N}_2)$ from $k_{1,0}(\text{M} = \text{He})$ and $k_{1,0}(\text{M} = \text{He})/k_{1,0}(\text{M} = \text{N}_2) = 0.55 \pm 0.05$ obtained from H_2O_2 thermal dissociation studies,⁷¹ at least for combustion modeling purposes.

5. Concluding Remarks

The potential energy hypersurface of the reaction $\text{OH} + \text{OH} (+\text{M}) \rightarrow \text{H}_2\text{O}_2 (+\text{M})$ has been investigated using high-level quantum chemistry methods. On the basis of the potential energy hypersurface obtained, the high-pressure limiting reaction rate coefficient was calculated using variable reaction coordinate transition-state theory, classical trajectory simulations, and a two-transition-state model. Available experimental data on the pressure dependence of the reaction with He and Ar as the bath gases were analyzed for the first time using a two-dimensional master equation. Our calculations describe well most of the experimental data, except the observations at 210 K for the reaction with He as the bath gas. To improve the description of the reaction, the experimental data should be extended to other temperatures and pressures, and new measurements with N_2 as the bath gas would be of value. Future theoretical studies should investigate the effect of angular momentum coupling of the electronic and rotational degrees of freedom in the OH radical in more detail.

Acknowledgment. This work was supported by the Research Council of Norway under Contract No. 173826/I30. The Norwegian Metacenter for Computational Science (Notur) is acknowledged for grants of computing time. Sandia is a multiprogram laboratory operated by Sandia Corporation, a Lockheed Martin Company, for the United States Department of Energy's National Nuclear Security Administration under Contract No. DE-AC04-94-AL85000. The authors are grateful to Dr. Stephen J. Klippenstein and Dr. Ahren W. Jasper for helpful discussions. Professors Jürgen Troe and V. G. Ushakov are acknowledged for making their paper available prior to publication.

References and Notes

- (1) O'Conaire, M.; Curran, H. J.; Simmie, J. M.; Pitz, W. J.; Westbrook, C. K. *Int. J. Chem. Kinet.* **2004**, *36*, 603–622.
- (2) Li, J.; Zhao, Z. W.; Kazakov, A.; Dryer, F. L. *Int. J. Chem. Kinet.* **2004**, *36*, 566–575.
- (3) Ströhle, J.; Myhrvold, T. *Int. J. Hydrogen Energy* **2007**, *32*, 125–135.
- (4) Lee, D.; Hochgreb, S. *Int. J. Chem. Kinet.* **1998**, *30*, 385–406.
- (5) Westbrook, C. K. *Proc. Combust. Inst.* **2000**, *28*, 1563–1577.
- (6) Mittal, G.; Sung, C. J.; Yetter, R. A. *Int. J. Chem. Kinet.* **2006**, *38*, 516–529.
- (7) Ströhle, J.; Myhrvold, T. *Combust. Flame* **2006**, *144*, 545–557.
- (8) Baulch, D. L.; Bowman, C. T.; Cobos, C. J.; Cox, R. A.; Just, T.; Kerr, J. A.; Pilling, M. J.; Stocker, D.; Troe, J.; Tsang, W.; Walker, R. W.; Warnatz, J. *J. Phys. Chem. Ref. Data* **2005**, *34*, 757–1397.
- (9) Caldwell, J.; Back, R. A. *Trans. Faraday Soc.* **1965**, *61*, 1939–1945.
- (10) Trainor, D. W.; von Rosenberg, C. W., Jr. *J. Chem. Phys.* **1974**, *61*, 1010–1015.
- (11) Zellner, R.; Ewig, F.; Paschke, R.; Wagner, G. *J. Phys. Chem.* **1988**, *92*, 4184–4190.
- (12) Forster, R.; Frost, M.; Fulle, D.; Hamann, H. F.; Hippler, H.; Schlegel, A.; Troe, J. *J. Chem. Phys.* **1995**, *103*, 2949–58.
- (13) Fulle, D.; Hamann, H. F.; Hippler, H.; Troe, J. *J. Chem. Phys.* **1996**, *105*, 1001–1006.
- (14) Kappel, C.; Luther, K.; Troe, J. *Phys. Chem. Chem. Phys.* **2002**, *4*, 4392–4398.
- (15) Troe, J. *J. Phys. Chem.* **1979**, *83*, 114–126.
- (16) Benson, S. W. *Acc. Chem. Res.* **1986**, *19*, 335–342.
- (17) Harding, L. B. *J. Phys. Chem.* **1991**, *95*, 8653–8660.
- (18) Koput, J.; Carter, S.; Handy, N. C. *J. Phys. Chem. A* **1998**, *102*, 6325–6330.
- (19) Kuhn, B.; Rizzo, T. R.; Luckhaus, D.; Quack, M.; Suhm, M. A. *J. Chem. Phys.* **1999**, *111*, 2565–2587.
- (20) Troe, J. *J. Chem. Phys.* **1977**, *66*, 4758–4775.
- (21) Brouwer, L.; Cobos, C. J.; Troe, J.; Duebal, H. R.; Crim, F. F. *J. Chem. Phys.* **1987**, *86*, 6171–6182.
- (22) Maergoiz, A. I.; Nikitin, E. E.; Troe, J. *J. Chem. Phys.* **1995**, *103*, 2083–2091.

- (23) Troe, J.; Ushakov, V. G. *Phys. Chem. Chem. Phys.* **2008**, *10*, 3915–3924.
- (24) Knowles, P. J.; Werner, H. J. *Chem. Phys. Lett.* **1985**, *115*, 259–267.
- (25) Werner, H. J.; Knowles, P. J. *J. Chem. Phys.* **1985**, *82*, 5053–5063.
- (26) Finley, J.; Malmquist, P.; Roos, B. O.; Serrano-Andres, L. *Chem. Phys. Lett.* **1998**, *288*, 299–306.
- (27) Werner, H. J. *Mol. Phys.* **1996**, *89*, 645–661.
- (28) Werner, H. J.; Knowles, P. J.; Lindh, R.; Manby, F. R.; Schütz, M.; Celani, P.; Korona, T.; Rauhut, G.; Amos, R. D.; Bernhardsson, A.; Berning, A.; Cooper, D. L.; Deegan, M. J. O.; Dobbyn, A. J.; Eckert, F.; Hampel, C.; Hetzer, G.; Lloyd, A. W.; McNicholas, S. J.; Meyer, W.; Mura, M. E.; Nicklass, A.; Palmieri, P.; Pitzer, R.; Schumann, U.; Stoll, H.; Stone, A. J.; Tarroni, R.; Thorsteinsson, T. *MOLPRO*, version 2006 1, a package of ab initio programs; 2006.
- (29) Becke, A. D. *J. Chem. Phys.* **1993**, *98*, 5648–5652.
- (30) Lee, C.; Yang, W.; Parr, R. G. *Phys. Rev. B* **1988**, *37*, 785–789.
- (31) Möller, C.; Plesset, M. S. *Phys. Rev.* **1934**, *46*, 618–622.
- (32) Raghavachari, K.; Trucks, G. W.; Pople, J. A.; Head-Gordon, M. *Chem. Phys. Lett.* **1989**, *157*, 479–483.
- (33) Frisch, M. J.; Trucks, G. W.; Schlegel, H. B.; Scusera, G. E.; Robb, M. A.; Cheeseman, J. R.; Zakrzewski, V. G.; Montgomery, J. A.; Stratmann, R. E., Jr.; Burant, J. C.; Dapprich, S.; Millam, J. M.; Daniels, A. D.; Kudin, K. N.; Strain, M. C.; Farkas, O.; Tomasi, J.; Barone, V.; Cossi, M.; Cammi, R.; Mennucci, B.; Pomelli, C.; Adamo, C.; Clifford, S.; Ochterski, J.; Petersson, G. A.; Ayala, P. Y.; Cui, Q.; Morokuma, K.; Malick, D. K.; Rabuck, A. D.; Raghavachari, K.; Foresman, J. B.; Cioslowski, J.; Ortiz, J. V.; Baboul, A. G.; Stefanov, B. B.; Liu, G.; Liashenko, A.; Piskorz, P.; Komaromi, I.; Gomperts, R.; Martin, R. L.; Fox, D. J.; Keith, T.; Al-Laham, M. A.; Peng, C. Y.; Nanayakkara, A.; Gonzalez, C.; Challacombe, M.; Gill, P. M. W.; Johnson, B.; Chen, W.; Wong, M. W.; Andres, J. L.; Gonzalez, C.; Head-Gordon, M.; Replogle, E. S.; Pople, J. A. *Gaussian 98*, revision A.11; Gaussian, Inc.: Pittsburgh, PA, 2001.
- (34) Schmidt, M. W.; Baldridge, K. K.; Boatz, J. A.; Elbert, S. T.; Gordon, M. S.; Jensen, J. H.; Koseki, S.; Matsunaga, N.; Nguyen, K. A.; Su, S. J.; Windus, T. L.; Dupuis, M.; Montgomery, J. A. *J. Comput. Chem.* **1993**, *14*, 1347–1363.
- (35) General Atomic and Molecular Electronic Structure System (GAMESS); <http://www.msg.ameslab.gov/GAMESS/GAMESS.html>, (accessed September 7 2006).
- (36) Dunning, T. H. *J. Chem. Phys.* **1989**, *90*, 1007–1023.
- (37) Kendall, R. A.; Dunning, T. H.; Harrison, R. J. *J. Chem. Phys.* **1992**, *96*, 6796–6806.
- (38) Woon, D. E.; Dunning, T. H. *J. Chem. Phys.* **1994**, *100*, 2975–2988.
- (39) Halkier, A.; Helgaker, T.; Jorgensen, P.; Klopper, W.; Koch, H.; Olsen, J.; Wilson, A. K. *Chem. Phys. Lett.* **1998**, *286*, 243–252.
- (40) Wardlaw, D. M.; Marcus, R. A. *J. Chem. Phys.* **1985**, *83*, 3462–3480.
- (41) Georgievskii, Y.; Klippenstein, S. J. *J. Chem. Phys.* **2003**, *118*, 5442–5455.
- (42) Georgievskii, Y.; Klippenstein, S. J. *J. Phys. Chem. A* **2003**, *107*, 9776–9781.
- (43) Keck, J. C. *Adv. Chem. Phys.* **1967**, *13*, 85–121.
- (44) Klippenstein, S. J.; Georgievskii, Y.; Harding, L. B. *Proc. Combust. Inst.* **2002**, *29*, 1229–1236.
- (45) Harding, L. B.; Klippenstein, S. J.; Georgievskii, Y. *Proc. Combust. Inst.* **2005**, *30*, 985–993.
- (46) Georgievskii, Y.; Klippenstein, S. J. *J. Chem. Phys.* **2005**, *122*, 194103.
- (47) Miller, J. A.; Klippenstein, S. J.; Raffy, C. J. *Phys. Chem. A* **2002**, *106*, 4904–4913.
- (48) Miller, J. A.; Klippenstein, S. J. *J. Phys. Chem. A* **2004**, *108*, 8296–8306.
- (49) Miller, J. A.; Klippenstein, S. J. *J. Phys. Chem. A* **2006**, *110*, 10528–10544.
- (50) Klippenstein, S. J.; Wagner, A. F.; Dunbar, R. C.; Wardlaw, D. M.; Robertson, S. H.; Miller, J. A. *VARIFLEX*, version 1.14m; 2005.
- (51) Miller, J.; Klippenstein, S. J. *J. Phys. Chem. A* **2000**, *104*, 2061–2069.
- (52) Pitzer, K. S. *J. Chem. Phys.* **1946**, *14*, 239–243.
- (53) Pitzer, K. S.; Gwinn, W. D. *J. Chem. Phys.* **1942**, *10*, 428–440.
- (54) Paul, P. H. *DRFM: A new package for the evaluation of gas-phase transport properties*, Technical Report SAND98-8203; Sandia National Laboratories: Livermore, CA, 1997.
- (55) Luo, X.; Fleming, P. R.; Rizzo, T. R. *J. Chem. Phys.* **1992**, *96*, 5659–5667.
- (56) Johnson, R. D., III, Ed. NIST Computational Chemistry Comparison and Benchmark Database, NIST Standard Reference Database Number 101, Release 12, 2005; <http://srdata.nist.gov/cccbdb> (accessed December 15, 2007).
- (57) Helgaker, T.; Gauss, J.; Jorgensen, P.; Olsen, J. *J. Chem. Phys.* **1997**, *106*, 6430–6440.

- (58) Redington, R. L.; Olson, W. B.; Cross, P. C. *J. Chem. Phys.* **1962**, *36*, 1311–1326.
- (59) Koput, J. J. *Mol. Spectrosc.* **1986**, *115*, 438–441.
- (60) Beaudet, R. A.; Poynter, R. L. *J. Phys. Chem. Ref. Data* **1978**, *7*, 311–362.
- (61) Mozurkewich, M.; Benson, S. W. *J. Phys. Chem.* **1984**, *88*, 6429–6435.
- (62) Greenwald, E. E.; North, S. W.; Georgievskii, Y.; Klippenstein, S. J. *J. Phys. Chem. A* **2005**, *109*, 6031–6044.
- (63) Georgievskii, Y.; Klippenstein, S. J. *J. Phys. Chem. A* **2007**, *111*, 3802–3811.
- (64) Klippenstein, S. J.; Georgievskii, Y.; Harding, L. B. *Phys. Chem. Chem. Phys.* **2006**, *8*, 1133–1147.
- (65) Jasper, A. W.; Klippenstein, S. J.; Harding, L. B. *J. Phys. Chem. A* **2007**, *111*, 8699–8707.
- (66) Sellevåg, S. R.; Georgievskii, Y.; Miller, J. A. *J. Phys. Chem. A* **2008**, *112*, 5085–5095.
- (67) Jasper, A. W.; Klippenstein, S. J.; Harding, L. B.; Ruscic, B. *J. Phys. Chem. A* **2007**, *111*, 3932–3950.
- (68) Jasper, A. W.; Klippenstein, S. J. Personal communication.
- (69) Herzberg, G. *Molecular Spectra and Molecular Structure. I. Spectra of Diatomic Molecules*, 2nd ed.; Dvan Nostrand Company, Inc.: Toronto, New York, London, 1950.
- (70) Atkinson, R.; Baulch, D. L.; Cox, R. A.; Crowley, J. N.; Hampson, R. F.; Hynes, R. G.; Jenkin, M. E.; Rossi, M. J.; Troe, J. *Atmos. Chem. Phys.* **2004**, *4*, 1461–1738.
- (71) Baldwin, R. R.; Brattan, D. *Proc. Combust. Inst.* **1960**, *8*, 110–119.

JP8110524